Variability of Comptonized X-ray spectra of a super-Eddington accretor: Approach using Boltzmann radiation transport

Takumi OGAWA,[1,*] Ken OHSUGA,[1] Yoshihiro MAKINO,[2] and Shin MINESHIGE[3]

[1]Center for Computational Sciences, University of Tsukuba, 1-1-1 Tennodai, Tsukuba, Ibaraki 305-8577, Japan
[2]Graduate School of Science, Kyoto University, Kitashirakawa-Oiwake-cho, Sakyo-ku, Kyoto, Kyoto 606-8502, Japan
[3]Department of Astronomy, Kyoto University, Kitashirakawa-Oiwake-cho, Sakyo-ku, Kyoto, Kyoto 606-8502, Japan

*E-mail: takumi@ccs.tsukuba.ac.jp

Abstract

We investigate the radiation fields around super-Eddington accretion flow, in which multiple inverse-Compton scattering plays a principal role, by using newly developed code describing Boltzmann radiation transfer in the Schwarzschild space-time. We apply this code to post-processing spectral calculations based on general relativistic, radiation magnetohydrodynamic simulation data to obtain X-ray spectra seen from various viewing angles. The radiation fields are distinctively separated into a funnel region with an opening angle of $\sim 30^\circ$, which is full with hot (gas temperature of $T > 10^8$ K), tenuous, and high-velocity plasmas, and surrounding cooler ($T \sim 10^7$ K) and optically thick outflow regions. Accordingly, there is a clear tendency that the smaller the viewing angle, the harder the spectra. In particular, hard photons with several tens of keV are observable only by observers at viewing angles less than $\sim 30^\circ$, consistent with past spectral studies based on simulations. Further, we investigate how the spectra are varied by a flare occurring in the innermost region, finding that the variation amplitude grows as the photon energy increases and that the harder photons emerge more quickly than softer photons. The observational implications on long-term spectral variability of ultra-luminous X-ray sources are briefly discussed.

Key words: accretion, accretion disks — radiation: dynamics — stars: black holes

1 Introduction

How to accurately solve radiation transfer equations? This is one of the most fundamental issues in astrophysics, since we can obtain rich information mainly via detecting electromagnetic wave radiation from astrophysical objects. Radiation is, however, not only a means of observation; it can also transport energy and momentum, thereby being able to have a significant impact on the environment around a radiating source and even on the media inside the source. Radiation can heat up gas (if absorbed and/or Compton upscattered) or cool down gas (if Compton down-scattered). It can also push material by asserting radiation-pressure or line-driven force. Good examples are stellar wind, which affects stellar evolution; and accretion disk outflow, which controls disk activities; and so on.

Let us focus on the cases of accretion disks around black holes. We soon notice that it is impossible to discuss X-ray

emission properties without Comptonization. Seed photons emitted from a cool and dense disk body are up-scattered by hot electrons existing around the disk to produce characteristic spectral features, such as hard power-law components and/or spectral humps. Two main sites are known to produce hard X-rays via inverse Compton scattering: low accretion-rate flow or the so-called radiatively inefficient accretion flow [RIAF; see chapter 9 of Kato, Fukue, and Mineshige (2008) and the references therein], and accretion disk coronae above and below sub-Eddington flow (see, e.g., Liang & Nolan 1984; Haardt & Maraschi 1991; Kato et al. 2008).

In both cases, the system has high-temperature (corresponding to a photon energy of $\sim 100\,\mathrm{keV}$) ionized gases around the central object. The Thomson optical depth is typically $\tau_{es} \sim 1$ and the Compton y-parameter is of the order of unity.

We wish to note that Comptonization should also be critical in super-Eddington accretors, since the strong radiation from the disk can blow off a large amount of gas to form mildly relativistic, uncollimated hot outflow so that the photons emitted from the underlying disk body can experience inverse Compton scattering when passing through the hot outflow (Kawashima et al. 2009). In contrast with the two sites mentioned above (i.e., RIAFs and disk coronae), Comptonizing outflow is characterized by (relatively) low-temperature ($\sim$ a few keV), optically thick ($\tau_{es} \sim 2$–5) Comptonization (e.g., Kitaki et al. 2017). Therefore, multiple scatterings dominate over single scatterings there.

Precise modeling of the Compton scattering process should be a critical issue but it is not an easy task, especially for relativistic plasmas under strong gravity. Several semi-analytic or simple numerical approaches are known for calculating radiation transfer with Compton scattering in accretion flow; see Rybicki and Lightman (1979) and references therein. However, more accurate and more realistic transfer calculations are now required, since high-resolution spectral data are now available thanks to the rapid progress in observational instrumentation (e.g., NuStar, etc.).

The Monte Carlo method is the most widely used, powerful tool for calculating radiation transfer with Compton scattering (e.g., Pozdnyakov et al. 1977; Dolence et al. 2009; Kawashima et al. 2012; Mościbrodzka et al. 2014). The great advantage of this method is that it can relatively easily calculate the scattering process, which is very complex in high-temperature gas layers and/or in a scattering medium moving with relativistic speed. In this method, we deal with statistics of the trajectory of photon packets in phase space; that is, photons experience Compton scattering with electrons, obeying the a priori prescribed statistics. The disadvantage of the Monte Carlo approach, however, is that the precision is limited by the photon statistics.

This limitation appears to be most severe when we handle photons with much higher energy than the seed photons, since the number of the former (up-scattered) photons could be very small, leading to rather poor statistics. Other disadvantages are difficulty in time-dependent calculation, lack of stimulated Compton scattering, and spatial resolution of physical quantities, although there are some studies of time-dependent or spatially resolved Monte Carlo calculations (see, e.g., Kinch et al. 2016; Ryan & Dolence 2020).

Another approach is solving the Boltzmann radiation transport equation to obtain the distribution function of photons in six-dimensional space: three-dimensional (3D) real space and 3D momentum space; see, e.g., Sumiyoshi and Yamada (2012), Nagakura, Sumiyoshi, and Yamada (2014), and Takahashi and Umemura (2017). The merit of this approach is its capability of simulating the time evolution of the medium, since we know the distribution function at all the spatial points and can thus calculate the feedback effects on the interacting medium. Another advantage is that this method can naturally be connected to the radiation hydrodynamics (RHD) simulation software, which will make it possible to perform frequency-dependent RHD simulations in future. The weak point of this method is a difficulty in calculating the Compton scattering process, since it is highly complicated when bulk and/or thermal velocities are relativistic or when we consider the high-energy regime. Another concern is the treatment of multiple scatterings. The scattering timescale is generally much shorter than that of the fluid or light crossing time. Usually, the time interval Δt is determined by the light crossing time and so the gas–radiation interaction term should be calculated by the implicit method. Then, the number experiencing scattering in one time-step should be much smaller than in the realistic case, since the scattering kernel describes only a single scattering. That is, multiple scattering cannot be precisely calculated by Boltzmann solver calculations, especially when the time interval Δt is taken to be much longer than the scattering timescale.

To summarize, the Monte Carlo method is easier to handle but has difficulty in solving time-dependent problems, while the Boltzmann method is advantageous in solving time-dependent problems but does not easily properly calculate multiple scattering processes. In the present study, therefore, we propose a new methodology to combine these two methods, and we apply our method to solving the problem of low-temperature, optically thick Comptonization as realized in super-Eddington flow. On the basis of the probability function of single scattering calculated by the Monte Carlo method, we can reconstruct the probability function of multiple scattering. The time evolution is then solved by the Boltzmann equation,
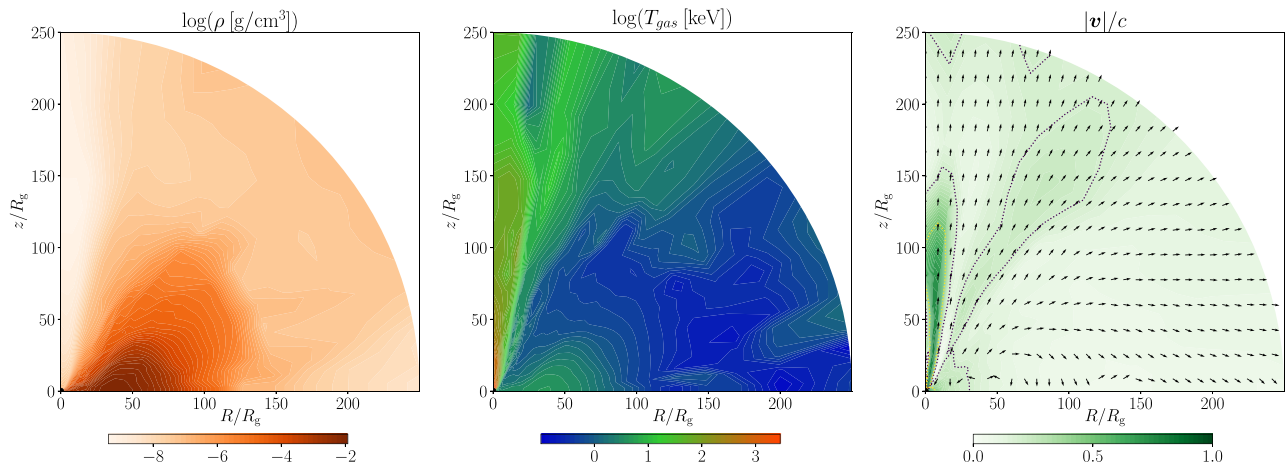
Fig. 1. Time-averaged GRRMHD data in a quasi-steady state (Takahashi et al. 2018). Color contours of the gas density, the gas temperature, and the gas velocity are displayed in the left, middle, and right panels, respectively. The right panel is overlaid with the velocity vectors. The black (yellow) dotted contour lines in the right panel indicate the loci of $|v/c| = 0.2$ (0.5). (Color online)

and the source term is calculated by the probability function of multi-scatterings. This enables us to calculate time-dependent radiation fields with multiple thermal/bulk Compton scatterings. The present study will mark an important milestone towards the construction of frequency-dependent general relativistic, radiation magnetohydrodynamic (GRRMHD) simulation code for accretion flow in a general context. We first explain the basic methodology in section 2, and then show the results of typical cases in section 3. The final section is devoted to a discussion.

2 Method

In the present study we have developed new code for a grid-based Boltzmann solver of the radiation transfer, incorporating the Compton scattering process, in the curved space-time described by the Schwarzschild metric, and we calculate the observed spectra of super-Eddington accretion flow and outflow by post-processing. We set $G = c = 1$ so that the units of the length scale are $1M = 15(M/10 M_\odot)$ km and those of the timescale are $1M = 5 \times 10^{-5}(M/10 M_\odot)$ s.

2.1 GRRMHD background data

We use the GRRMHD data (ρ, T, v) for calculating the radiation field in our simulation, where ρ is the density, T is the temperature, and v is the velocity of the fluid. These data are obtained by the 2D axisymmetric simulations of Takahashi, Mineshige, and Ohsuga (2018), who solved the GRRMHD equations in polar coordinates on the basis of the Kerr–Schild metric around a non-spinning black hole. Here, we summarize the properties of the GRRMHD

simulation data used

- The simulation domain $(r\,[M],\ \theta\,[\mathrm{rad}]) \in [1.96,\ 245] \times [0,\ \pi]$ is divided into 264×264 cells. A $10\,M_\odot$ black hole was placed at the origin $(r = 0)$.
- The simulation was started from an equilibrium torus composed of pure hydrogen plasma threaded with single poloidal magnetic fields. The inner edge of the initial torus was at $r = 20\,M$ and the pressure maximum at $r = 33\,M$.
- The super-Eddington accretion flow and radiatively driven outflows were reproduced. The mass accretion rate onto the central black hole was about $300\,L_{\mathrm{Edd}}$ in the quasi-steady state, which was achieved after an elapsed time of $3000\,M$.
- In the quasi-steady state, no unphysical flares (which are occasionally observed in simulations based on the M1 scheme) or artificial abrupt heating occurred.

We employ simulation data that are time-averaged over the time span $t = 3000$–$3300\,M$ (in the quasi-steady state). Figure 1 shows, from left to right, contour maps of the density, temperature, and velocities overlaid with the velocity vectors. We see a two-phased structure composed of a dense, low-temperature torus region and a tenuous, high-temperature outflow region.

Before performing the radiation transfer calculation we transformed the values described in the Kerr–Schild metric into those in the Schwarzschild metric. We also reduced the numerical resolution of the data from 264×264 grid points to 32×64 grid points because of the limitations of the calculation resource. The electron temperature in our calculation is assumed to be equal to the proton temperature, for simplicity (this approximation will be discussed in subsection 4.4).

2.2 Basic equation

The basic equation that we solve in the present paper is the conservative form of the Boltzmann equation in the Schwarzschild coordinates (t, r, θ, φ) derived by Shibata et al. (2014),

$$
\left(1 - \frac{2M}{r}\right)^{-1/2} \frac{\partial f}{\partial t} + \frac{1}{r^2} \frac{\partial}{\partial r}\left[f \cos\overline{\theta}\, r^2 \left(1 - \frac{2M}{r}\right)^{1/2}\right]
$$
$$
+ \frac{1}{r \sin\theta} \frac{\partial}{\partial \theta}\left(f \sin\theta \sin\overline{\theta} \cos\overline{\varphi}\right)
$$
$$
+ \frac{1}{r \sin\theta} \frac{\partial}{\partial \varphi}\left(f \sin\overline{\theta} \sin\overline{\varphi}\right)
$$
$$
- \frac{1}{\nu^2} \frac{\partial}{\partial \nu}\left[f \nu^3 \cos\overline{\theta}\, \frac{M}{r^2}\left(1 - \frac{2M}{r}\right)^{-1/2}\right]
$$
$$
- \frac{1}{\sin\overline{\theta}} \frac{\partial}{\partial \overline{\theta}}\left[f \sin^2\overline{\theta}\, \frac{r - 3M}{r^2}\left(1 - \frac{2M}{r}\right)^{-1/2}\right]
$$
$$
- \frac{\partial}{\partial \overline{\varphi}}\left(f \frac{\cot\theta}{r} \sin\overline{\theta} \sin\overline{\varphi}\right) = S_{\rm rad}, \qquad (1)
$$

where f, M, and $S_{\rm rad}$ are the distribution function of photons, the mass of the central black hole, and the source term via gas–radiation interactions, respectively. The set $(\nu, \overline{\theta}, \overline{\varphi})$ represents the coordinates in the momentum space of photons, in which ν is the frequency of photons measured by an Eulerian observer, $\overline{\theta}$ is the angle between the direction of the photon propagation and the r-direction, and $\overline{\varphi}$ is the angle between the θ-direction and the projected photon momentum vector on the plane perpendicular to the r-direction. Note that we use fluid data provided by the 2D axisymmetric simulation so that the derivative $\partial/\partial \varphi$ vanishes.

We solve the left-hand side of equation (1) (i.e., the advection term) by the second-order upwind method with the min-mod limiter (although it is slightly modified, as will be shown in subsection 2.4 and the Appendix). The right-hand side, which is the source term of gas–radiation interactions, is solved using interaction tables (see subsection 2.5).

2.3 Simulation setup

We perform the radiation transfer simulations within the 5D simulation domain of $r\,[M] = 2.1$–250, $\theta = 0$–π, $h\nu\,[{\rm keV}] = 0.01$–500, $\overline{\theta} = 0$–π, and $\overline{\varphi} = 0$–2π. The grid points are uniformly distributed in the θ-, $\overline{\theta}$-, and $\overline{\varphi}$-directions, and uniformly distributed in logarithm in the ν- and r-directions. The numbers of grid points are $(N_r, N_\theta, N_\nu, N_{\overline{\theta}}, N_{\overline{\varphi}}) = (32, 64, 50, 9, 8)$. As the opacity sources, bremsstrahlung by a pure hydrogen plasma and electron scattering (with a Klein–Nishina cross-section) are included.

At the inner and outer boundaries, $r\,[M] = 2.1$ and 250, we employ free (no-gradient) boundary conditions for the outgoing radiation, and the incoming radiation is set to zero. We use the reflective boundary condition at $\theta = 0$ and π, as well as at $\overline{\theta} = 0$ and π. At the boundaries of the frequency grid we employ the dumping boundary condition (i.e., we assign small values there). We use the periodic boundary condition at $\overline{\varphi} = 0$ and 2π.

Initially we assume no radiation field in the whole simulation domain and calculate the time evolution of the radiation fields by solving equation (1).

2.4 Advection terms

In our simulations, the time interval Δt is determined by the Courant–Friedrichs–Lewy condition for the advection terms. Hereafter, we write each grid in the 5D real-momentum space by $(r_j, \theta_k, \nu_i, \overline{\theta}_m, \overline{\varphi}_n)$. The grid of the photon frequency is set regularly in the fluid-rest frame for convenience in calculating the source term, since the scattering table which we refer to is defined in the fluid-rest frame. Note that the scattering probability depends on the scattering angle and the frequency of an incoming photon in the fluid-rest frame. In contrast, the grid for the direction of the photon propagation ($\overline{\theta}$ and $\overline{\varphi}$) is set regularly not in the fluid-rest frame but in the laboratory frame, since then the advection term can be solved more easily and the grid regularity in the fluid-rest frame does not facilitate this calculation.

This sort of grid setting is the same as that adopted by Nagakura, Sumiyoshi, and Yamada (2014). In such a grid setting the grid of frequency in the laboratory frame is different for each grid, $(r, \theta, \phi, \overline{\theta}, \overline{\varphi})$— see the Appendix for more details. For instance, if two neighboring grids have different fluid velocities, the ith frequency in the laboratory frame (which corresponds to the ith frequency in the fluid-rest frame, ν_i) is different. This is because the frequency in the laboratory frame depends on the Doppler factor, which is a function of the direction of the photon propagation and the fluid velocity. We thus need to turn the variable frequency grid into a regular one in the laboratory frame to solve the advection terms.

The numerical procedures can be summarized as:

1. Interpolate the distribution function in the co-moving regular grid points to obtain the values in the laboratory regular grid points.
2. Calculate numerical fluxes in each direction other than the frequency differential in the laboratory regular grid points.
3. Interpolate the numerical fluxes in the laboratory regular grid to obtain the values in the co-moving regular

grid and evaluate the numerical flux in the frequency direction.

4. Update the values of the radiation intensity by using the numerical fluxes obtained in step 3.

More detailed procedures are presented in the Appendix.

2.5 Source term

Although the distribution function should be updated by solving $(1-2\,M/r)^{-1/2}\partial f/\partial t = S_{\rm rad}$, evaluating the source term is basically difficult, especially when the Compton scattering process is involved, because information in any position of the 3D momentum space $(\nu, \bar{\theta}, \bar{\varphi})$ is coupled and entangled with each other, unlike the cases with absorptions and/or Thomson (and other elastic) scattering only. In other words, the non-elastic scattering process (e.g., Compton scattering or even Thomson scattering by thermal electrons) can be considered as the flow in the 3D momentum space of photons, while the elastic scattering (e.g., Thomson scattering by electrons, whose motion is negligibly slow) can be considered as the flow on the constant-energy surface, which has a 2D structure, in the 3D momentum space of photons. It is thus difficult to integrate the scattering kernel whenever the Compton scattering is effective.

For this reason, we calculate two interaction tables $(S^{\rm abs,scat}_{i,m,n;i',m',n'}$ and $S^{\rm emit}_{i,m,n})$ beforehand and update the distribution function by

$$f(\nu_i, \bar{\theta}_m, \bar{\varphi}_n; t + \Delta t) = \sum_{i',m',n'} S^{\rm abs,scat}_{i,m,n;i',m',n'} f(\nu_{i'}, \bar{\theta}_{m'}, \bar{\varphi}_{n'}; t)$$
$$+ S^{\rm emit}_{i,m,n}. \quad (2)$$

The first term on the right-hand side corresponds to the photons travelling from $(\nu_{i'}, \bar{\theta}_{m'}, \bar{\varphi}_{n'})$ to $(\nu_i, \bar{\theta}_m, \bar{\varphi}_n)$ in 3D momentum space while suffering from absorption and scattering. Also, $S^{\rm emit}_{i,m,n}$ means an increase in the distribution function by emission. In the following subsections, we introduce how we obtain $S^{\rm abs,scat}_{i,m,n,i',m',n'}$ and $S^{\rm emit}_{i,m,n}$.

We omit the subscripts indicating the spatial grid points here, since the gas–radiation interaction occurs in a local grid.

2.5.1 Single scattering function

To prepare for numerical calculations we first estimate the single scattering distribution function by Monte Carlo simulations, in which we take into account the Compton scattering by thermal electrons and the Klein–Nishina cross-section. These Monte Carlo simulations provide us with the total cross-section $\kappa_{\rm total}(\nu_{\rm in}, T_{\rm e})$ and the single scattering distribution function $P_1(\nu_{\rm out}, \Theta, \nu_{\rm in}, T_{\rm e})$, where $\nu_{\rm out}$, Θ, $\nu_{\rm in}$, and $T_{\rm e}$ are the photon frequency after the scattering, the angle between the incoming photon direction and the outgoing

photon direction, the frequency of the incoming photon, and the electron temperature.

For a set of $(\nu_{\rm in}, T_{\rm e})$, we perform Monte Carlo simulations with 10^8 injected photons, and scattered photons are collected for each $\Delta\Theta = \pi/100$ bin in the range $0 \le \Theta \le \pi$ and each $\Delta\log h\nu_{\rm out}\,[{\rm keV}] = 0.055$ bin in the range $4 \times 10^{-7} \le h\nu_{\rm out}\,[{\rm keV}] \le 4 \times 10^4$. We repeat the above procedure 200×30 times for each pair of $(\nu_{\rm in}, T_{\rm e})$ in order to cover the ranges $4 \times 10^{-7} \le h\nu_{\rm in}\,[{\rm keV}] \le 4 \times 10^4$ and $10^{-3} \le T_{\rm e}\,[{\rm keV}] \le 10^3$.

2.5.2 Interaction table for multi-scattering and absorption

Using the single scattering distribution function P_1 obtained above, we produce the table for the multiple scattering and absorption. The time interval Δt in the present simulations becomes much larger than the scattering timescale in the high-density cells where the multiple scattering intricately changes the distribution function. Thus, we employ a sub-time interval, $\Delta t_{\rm scat}\,(= \Delta t/N)$, to treat multi-scattering more accurately, where the controll parameter N is fixed to 7 in our simulations. We performed the same simulation with $N = 14$, finding no appreciable changes (less than 10%). By starting from $\tilde{f}^0 = \delta^i_{i0}\delta^m_{m0}\delta^n_{n0}$, we solve the equation

$$\tilde{f}^{l+1}(\nu_i, \bar{\theta}_m, \bar{\varphi}_n) = [1 - \phi(\nu_i, \bar{\theta}_m, \bar{\varphi}_n, T, \rho, \boldsymbol{v}, \Delta t_{\rm scat})]$$
$$\times [1 - \phi_{\rm abs}(\nu_i, \bar{\theta}_m, \bar{\varphi}_n, T, \rho, \boldsymbol{v}, \Delta t_{\rm scat})]$$
$$\times \tilde{f}^l(\nu_i, \bar{\theta}_m, \bar{\varphi}_n)$$
$$+ \sum_{i',m',n'} \phi[(\nu_{i'}, \bar{\theta}_{m'}, \bar{\varphi}_{n'}, T, \rho, \boldsymbol{v}, \Delta t_{\rm scat})]$$
$$\times [1 - \phi_{\rm abs}(\nu_{i'}, \bar{\theta}_{m'}, \bar{\varphi}_{n'}, T, \rho, \boldsymbol{v}, \Delta t_{\rm scat})]$$
$$\times P_1(\nu_i, \Theta_{m,n;m',n'}, \nu_{i'}, T)$$
$$\times \tilde{f}^l(\nu_{i'}, \bar{\theta}_{m'}, \bar{\varphi}_{n'})\Delta p^3_{i',m',n'} \quad (3)$$

for $i = 1\text{–}N_\nu$, $m = 1\text{–}N_{\bar{\theta}}$, $n = 1\text{–}N_{\bar{\varphi}}$, where $\tilde{f}$ is the working distribution function, ϕ is the scattering probability function, $\phi_{\rm abs}$ is the absorption probability function, $\Theta_{m,n;m',n'}$ indicates the angle between the photon directions of $(\bar{\theta}, \bar{\varphi}) = (\bar{\theta}_{m'}, \bar{\varphi}_{n'})$ and $(\bar{\theta}_m, \bar{\varphi}_n)$, and the superscript l denotes the number of iterations of the sub-time-step. It is notable that the scattering/absorption probability depends on the fluid velocity and the direction of photon propagation. After solving the above equation N times repeatedly, we obtain the table for multiple scattering and absorption as $S^{\rm abs,scat}_{i,m,n;i0,m0,n0} = \tilde{f}^N(\nu_i, \theta_m, \phi_n)$ for $i = 1\text{–}N_\nu$, $m = 1\text{–}N_{\bar{\theta}}$, $n = 1\text{–}N_{\bar{\varphi}}$.

By repeating the above procedure $N_\nu \times N_{\bar{\theta}} \times N_{\bar{\varphi}}$ times while changing $(\nu_{i0}, \bar{\theta}_{m0}, \bar{\varphi}_{n0})$, we obtain the full set of coefficients of $S^{\rm abs,\,scat}$ in equation (2). This is the table for multiple scattering and absorption.
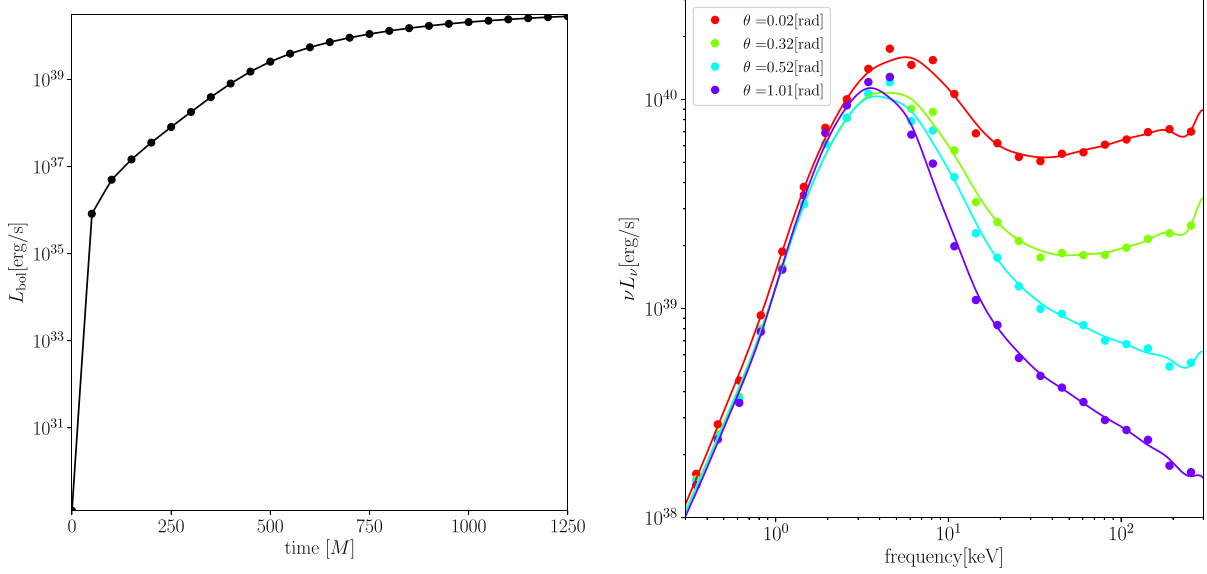
Fig. 2. Left: Time evolution of the total luminosity over the time span 0–1250 M. Right: Observed spectra (in the quasi-steady state) viewed by a distant observer located at angles of θ_{view} [radian] = 0.02 (~0°, red), 0.32 (~20°, green), 0.52 (~30°, blue), and 1.01 (~60°, purple). The closed circles denote the calculated data points, whereas the curves represent the spline fits to the three-point average of the data points. (Color online)

2.5.3 Emission

In the previous subsection, the emitted photons during the time interval Δt_{scat} were not considered. The emitted photons also suffer from multiple scattering and absorption, so that the coefficient for the emission can be obtained by repeating the following equation N times:

$$
\begin{aligned}
\tilde{f}^{l+1}(\nu_i, \bar{\theta}_m, \bar{\varphi}_n) &= [1 - \phi(\nu_i, \bar{\theta}_m, \bar{\varphi}_n, T, \rho, \boldsymbol{v}, \Delta t_{\text{scat}})] \\
&\times \frac{\tilde{f}^l(\nu_i, \bar{\theta}_m, \bar{\varphi}_n) + \kappa_{\text{abs}}(\nu_i, \bar{\theta}_m, \bar{\varphi}_n, T, \boldsymbol{v})\rho \Delta t_{\text{scat}} B_\nu(T)}{1 + \kappa_{\text{abs}}(\nu_i, \bar{\theta}_m, \bar{\varphi}_n, T, \boldsymbol{v})\rho \Delta t_{\text{scat}}} \\
&+ \sum_{i',m',n'} \phi([\nu_{i'}, \bar{\theta}_{m'}, \bar{\varphi}_{n'}, T, \rho, \boldsymbol{v}, \Delta t_{\text{scat}}]) P_1(\nu_i, \Theta_{m,n;m',n'}, \nu_{i'}, T) \\
&\times \frac{\tilde{f}^l(\nu_{i'}, \bar{\theta}_{m'}, \bar{\varphi}_{n'}) + \kappa_{\text{abs}}(\nu_{i'}, \bar{\theta}_{m'}, \bar{\varphi}_{n'}, T, \boldsymbol{v})\rho \Delta t_{\text{scat}} B_\nu(T)}{1 + \kappa_{\text{abs}}(\nu_{i'}, \bar{\theta}_{m'}, \bar{\varphi}_{n'}, T, \boldsymbol{v})\rho \Delta t_{\text{scat}}} \Delta p^3_{i',m',n'} \quad (4)
\end{aligned}
$$

for $i = 1$–N_ν, $m = 1$–$N_{\bar{\theta}}$, $n = 1$–$N_{\bar{\varphi}}$ as $S^{\text{emit}}_{i,m,n} = \tilde{f}^N(\nu_i, \theta_m, \phi_n)$, where κ_{abs} is the opacity for the absorption, B_ν is the Planck function, and $\tilde{f}^0$ is set to be zero.

In the present simulations we investigate the time evolution of f using equation (2). The Monte Carlo simulations are necessary to produce the table, but not required for every step.

3 Results

3.1 Simulation overview

We calculate the observed luminosity at frequency ν seen from a viewing angle of θ_{view}, $L_\nu(\theta_{\text{view}}, t)$, by

$$
L_\nu(\theta_{\text{view}}, t) = 4\pi \int_{\{\theta,\bar{\theta},\bar{\varphi}\} \in \Lambda(\theta_{\text{view}})} I_\nu(t, r = r_{\text{out}}, \theta, \bar{\theta}, \bar{\varphi})\, dS, \quad (5)
$$

where the set $\Lambda(\theta_{\text{view}})$ contains all elements $(\theta, \bar{\theta}, \bar{\varphi})$ satisfying the condition where the direction determined by $(\theta, \bar{\theta}, \bar{\varphi})$ is parallel to the direction of the observer (θ_{view}) and where it is outward-directing on the outer boundary of the simulation domain, and the area element dS is that on the screen of the distant observer, and the bolometric

luminosity, $L_{\text{bol}}(t)$, by

$$
L_{\text{bol}}(t) = \frac{1}{2} \iint L_\nu(\theta_{\text{view}}, t)\, d\nu\, d(\cos\theta_{\text{view}}) \quad (6)
$$

at each time. Here, we assume that the photons go straight without suffering gravitational redshift outside the computational box, since the distance from the black hole is sufficiently far that the general relativistic (GR) effect is negligibly small. We plot how the bolometric luminosity grows, starting from the initial zero-luminosity state, in the left panel of figure 2. The bolometric luminosity reaches $\sim 10^{40}\,\text{erg s}^{-1}$ ($\sim 10\,L_{\text{Edd}}$) in four light crossing times (where we define the light crossing time to be $t_{\text{cross}} \equiv r_{\text{out}}/c = 250\,M$). We see that the radiation field settles down to a
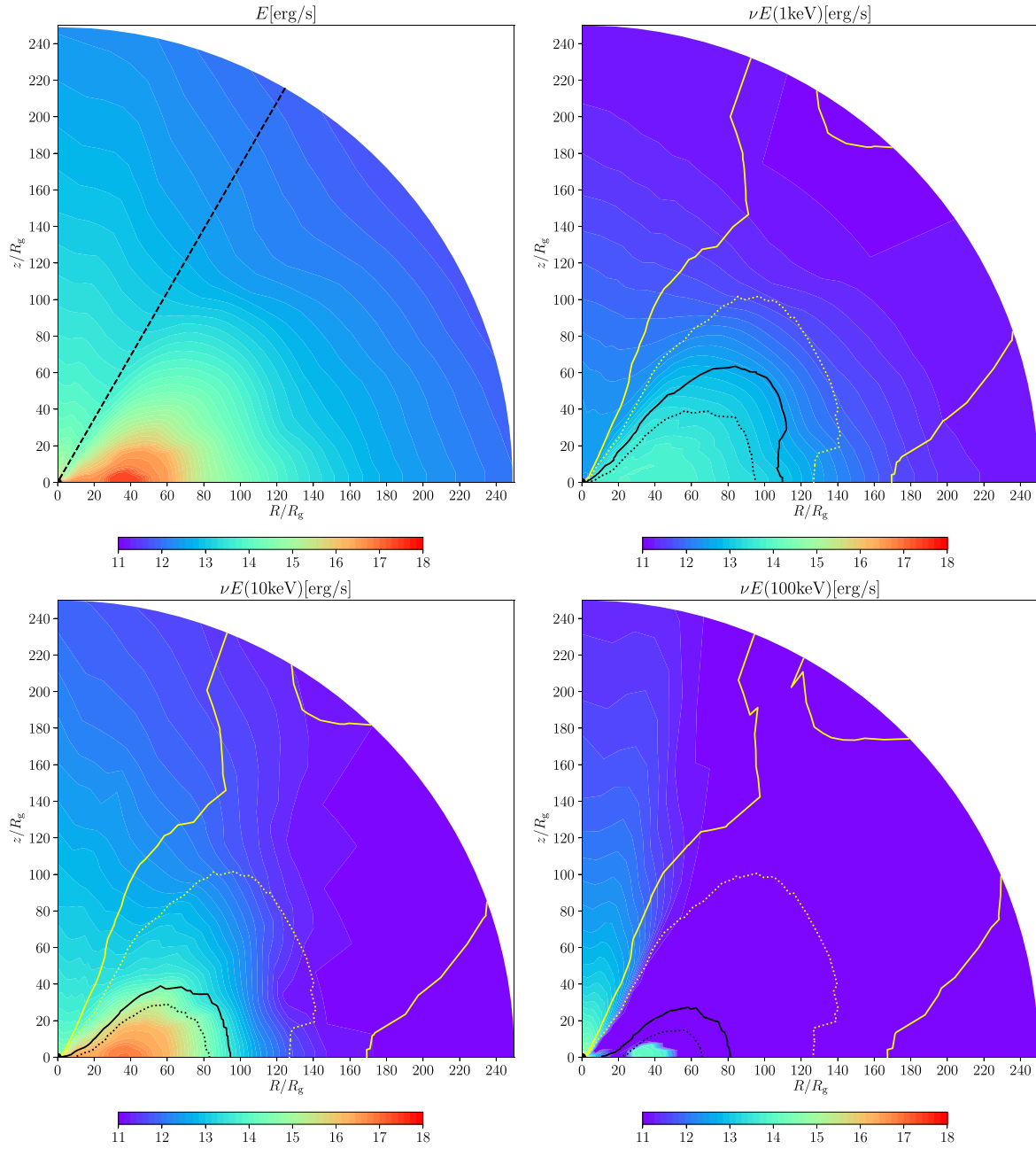
Fig. 3. Contour maps of the total radiation energy density (upper left) and the radiation density at different energy bins: 1 (upper right), 10 (bottom left), and 100 keV (bottom right). The lines in the last three panels indicate the loci of $\tau_{\rm eff} = 1$ and 10 (black solid and dotted lines), and $\tau_{\rm es} = 1$ and 10 (yellow solid and dotted lines). The dashed line in the upper left panel is the line with polar angle $\theta = 30°$, which indicates the approximate position of the funnel wall. (Color online)

quasi-steady state at $t > t_{\rm qss} \equiv 4t_{\rm cross}$ (see the left panel of figure 2).

The right panel of figure 2 shows the observed spectra in the quasi-steady state, $L_\nu(\theta_{\rm view}, t = t_{\rm qss})$ for various viewing angles. We see a clear trend that the larger the inclination angle, the lower the hard X-ray component, and hence the softer the spectrum. This can be easily understood, since the high-energy photons (with energy > 10 keV) are mostly generated in the funnel region. Therefore, they can be observed

only by a nearly face-on observer (with a viewing angle $\theta_{\rm view} \leq 30°$) and are not seen by a nearly edge-on observer, for whom they are effectively blocked by optically thick outflow. The lower-energy photons (with energy < 10 keV), by contrast, originate from the much wider region surrounding the funnel and disk, and hence are always observable: they can directly propagate even to an edge-on observer.

We next examine the two-dimensional distributions of the radiation energy density in the simulation box. The

upper left panel of figure 3 shows the color contours of the total radiation energy density (integrated over photon energy) overlaid with the total energy flux vectors, while the other three panels of figure 3 illustrate the color contours of the energy density of radiation with $\nu = 1$ (upper right), 10 (lower left), and 100 keV (lower right). The loci of the effective optical depth of $\tau_{\mathrm{eff}} = 1$ and 10 are indicated by the black solid and black dotted lines, respectively, while those of the Thomson optical depth of $\tau_{\mathrm{es}} = 1$ and 10 are indicated by the yellow solid and yellow dashed lines, respectively.

The strongest is the 10 keV emission from the optically thick disk region. (This is the reason why the total radiation energy density reaches its maximum value there.) Further, we find in the lower two panels that the high-energy photons, $\gtrsim 10$ keV, emerge from hot regions within the jet funnel region. Here, by the funnel region we mean the region which is full with hot ($T > 10^8$ K), tenuous (with Thomson optical depth $\tau_{\mathrm{es}} < 1$), and rapidly outflowing (with $v > 0.1\,c$) gas (Kitaki et al. 2017). Crudely, this funnel region has an opening angle of $30°$ (the region above the black dashed line in the upper left panel) and is surrounded by the slower (with velocity $v < 0.1\,c$) and denser outflow region. Such high-energy photons propagate along the polar axis or are advected by the optically thick outflow, which is launched from the inner hot region and propagates toward the direction of a polar angle of $20°$–$40°$. The 10 keV photons are produced mostly within the disk and some in the funnel, whereas the 1 keV photons originate from a much wider space in and around the disk. The photons emitted from the disk can effectively lose their energy via Compton scattering, whereas those from the funnel can partly leak into the slower and denser outflow region.

3.2 Dependence of intensity map on viewing angle and photon energies

We next show in figure 4 how the super-Eddington accretion flow and outflow look in X-rays to distant observers at different viewing angles (measured from the polar axis), θ_{view}. The upper panels show images of the flow seen from a viewing angle of $\theta_{\mathrm{view}} \sim 0°$ at photon energies of 1, 10, and 100 keV from left to right. In all the panels the polar cap region around $(x, y) = (0, 0)$ is brightest and the region around $\theta \sim 50°$ is the second brightest, about one third of the former. Although the emission from the latter is not so strong, it has a much wider area than the former.

The three panels in the middle row show the same but seen from $\theta_{\mathrm{view}} \sim 20°$. A large fraction of the hard photons ($\gtrsim 10$ keV) come from the funnel region, whereas lower-energy ones originate from more or less the entire region. The brightest region at 1 keV is the off-polar regions of

$\theta = 20°$–$50°$. The same trend can be seen in the bottom panels for the cases with $\theta_{\mathrm{view}} \sim 30°$. Since gas is rotating around the black hole, radiation tends also to go around the polar axis after undergoing multi-scattering, especially in the optically thick region. This effect can be clearly seen in the middle and lower rows of figure 4. From all the panels in figure 4 we understand that very high-energy emission (above a few tens of keV) is very sensitive to the viewing angle, while softer emission is not so sensitive to the viewing angle.

3.3 Comparison with isotropic scattering

In order to investigate the importance of anisotropic scattering effects dependent on photon energy in Compton scattering, we repeat the same radiative transfer simulation but adopting an isotropic scattering kernel; that is, we now use an angle-averaged scattering probability function, $P'(\nu, \nu', T) \equiv \int P_1(\nu, \Theta, \nu', T)\, d\Omega/4\pi$. For convenience, the superscript "iso" means a value obtained by simulation using the isotropic scattering kernel, and we write the relative difference of any physical quantity, Q, between the two simulations (one with anisotropic scattering kernel and the other isotropic) as $\epsilon_{\mathrm{R}}(Q) \equiv (Q - Q^{\mathrm{iso}})/Q$.

The middle panel of figure 5 shows the relative difference of the observed spectrum for several viewing angles. The biggest difference is found at photon energies of ~ 10 keV, especially when the viewing angle is large. The maximum relative difference amounts to $\sim 20\%$ at around 10 keV. This difference stems from the different angular dependence of the scattering, but we wish to understand for which region a big difference arises. We carefully compare the images for the cases with and without anisotropic scattering effects, and find the biggest difference in the funnel region, especially for higher-energy photons. Further, we find a large difference in F_{r}, the radial component of the radiation flux. Interestingly, F_{r} grows upward, since high-energy photons are generated within the funnel (see the lower right panel of figure 3). Since the funnel wall region corresponds to the region where the fluid velocity is relatively higher, we suggest that these big differences may be consequences of the bulk Comptonization rather than the thermal Comptonization (see next subsection).

3.4 Contribution of bulk Comptonization

To check the importance of the bulk Comptonization, we repeat the same transfer simulation but excluding the bulk Compton scattering, by assigning zero velocity in the funnel region (with $\theta < 30°$). The calculated observed spectrum shows the biggest difference in the high-energy regime (see the right panel of figure 5). We can understand this trend
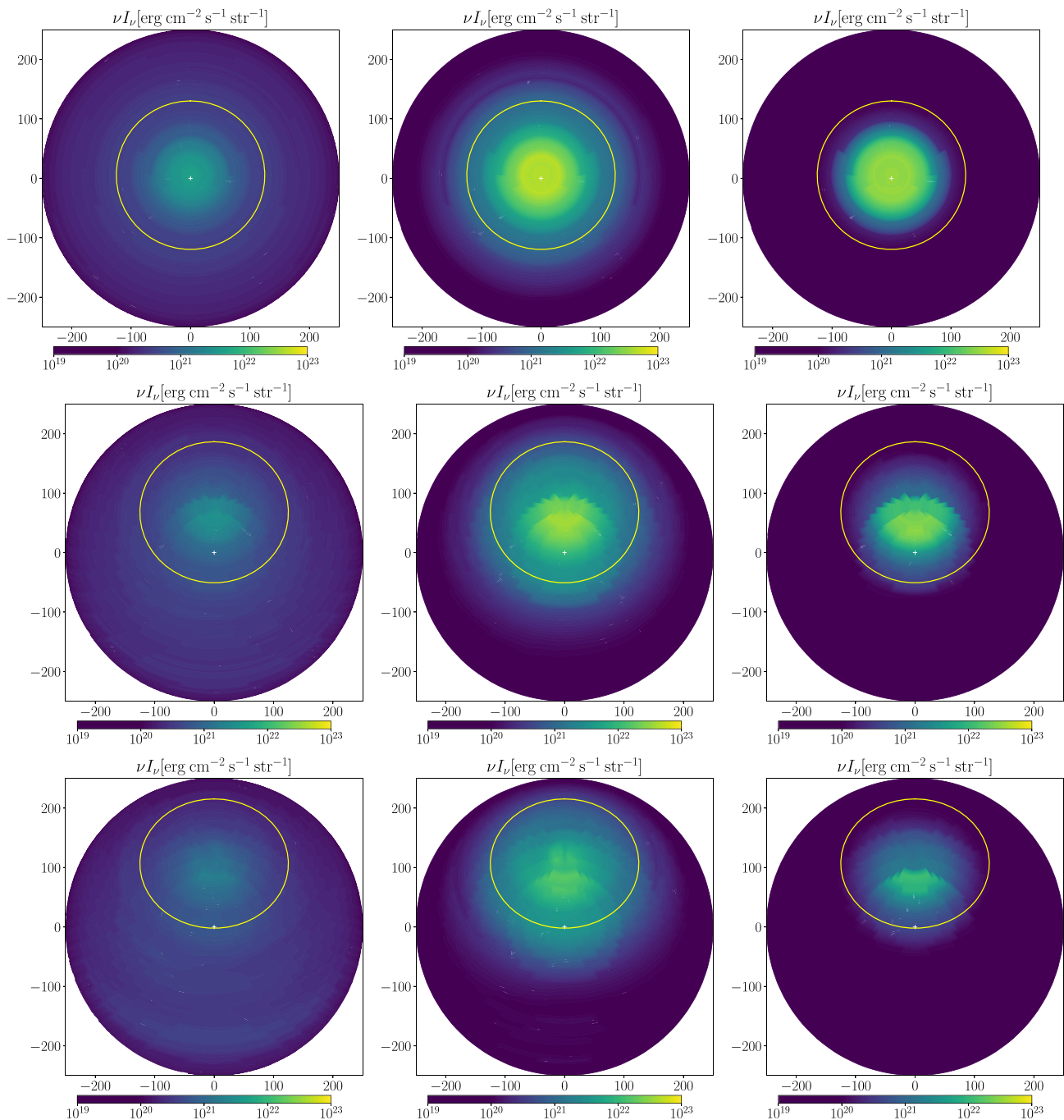
Fig. 4. Images observed by a distant observer located at viewing angles (measured from the polar axis) of 0° (upper row), 20° (middle row), and 30° (bottom row) for photon energies of 1 (left column), 10 (middle column), and 100 keV (right column). The yellow line represents the intersection between the funnel wall (defined by the polar angle of $\theta = 30°$, see figure 1) and the outer boundary of the simulation box. The plus marker indicates the position of the origin, where the black hole is located. (Color online)

through figure 4, which shows that the high-energy photons ($\gtrsim 20\,\mathrm{keV}$) come from the interior of the funnel region for all viewing angles, where the bulk Compton scattering plays an important role. We therefore conclude that the high-energy photons are mainly made by the bulk Compton scattering near the funnel wall. By contrast, we see smaller differences in the low-energy spectrum, since low-energy

photons ($\lesssim 10\,\mathrm{keV}$) are generated outside the funnel, especially in the disk and surrounding slow outflow region (see the upper right panel of figure 3).

3.5 Spectral variability caused by a flare

It is well known that black hole objects commonly exhibit significant degrees of variability on various timescales. Such
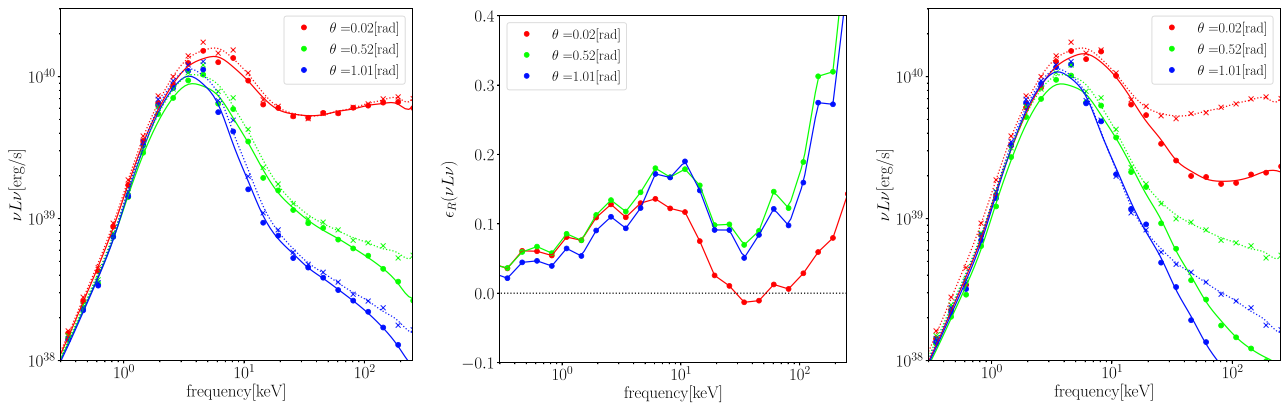
Fig. 5. Left: Angular dependence of the observed spectrum in the fiducial model (with anisotropic scattering effects, dashed line) and that in the isotropic model (solid line). Middle: Relative errors of the observed spectrum, $\epsilon_R(\nu L\nu)$, between the fiducial model and the isotropic model. Right: As the left panel but for the case with no bulk Comptonization. The closed circles denote the calculated data points, while the solid curves in the left and right panels are the third-order spline fit to the data points. (Color online)

variabilities were already known in the dawn of X-ray astronomy (e.g., Oda et al. 1971), but their origin remains an open issue (see, e.g., Done et al. 2007; Falanga et al. 2015, and references therein). One of the most promising possibilities is assembly of flare-like events (Galeev et al. 1979). The frequent occurrence of magnetic flares is very likely in hot accretion flow like RIAF and in an accretion disk corona, since both seem to be composed of hot magnetized plasmas, like solar coronae. This has led to the idea of the lamppost model, in which a compact hard X-ray emitting source above a black hole illuminates a surrounding accretion disk (e.g., Martocchia & Matt 1996; Miniutti & Fabian 2004). It is thus interesting to see how the spectra change with time in response to a flaring event occurring in the innermost region.

Prompted by such considerations, we calculate the spectral variation of a super-Eddington accretor in response to a sudden heating of the innermost zone caused by a flaring event (i.e., magnetic reconnection). Using the simulation data at $t_0 = 1000\,M$, in which a quasi-steady state is achieved, we suddenly raise the gas temperature $T_{\rm gas}$ in the innermost funnel region ($r < 20\,M$ and $\tau_{\rm es} < 10$, where $\tau_{\rm es}$ is the optical depth by electron scattering calculated from the polar axis) by a factor of 10 for a time interval of $200\,M$ (corresponding to 10 times the light crossing time of the flare region), and then suddenly drop the gas temperatures to their original values (we do not consider any specific mechanisms but simply assume sudden cooling; this issue will be improved in a future work). We calculate how the spectrum changes with time with the occurrence and termination of the flare, and show the results in figure 6.

As is clearly shown in this figure, the spectra are largely deformed during the flare, especially in the hard X-ray range above ∼20 keV. Notably, such variations are sensitive to
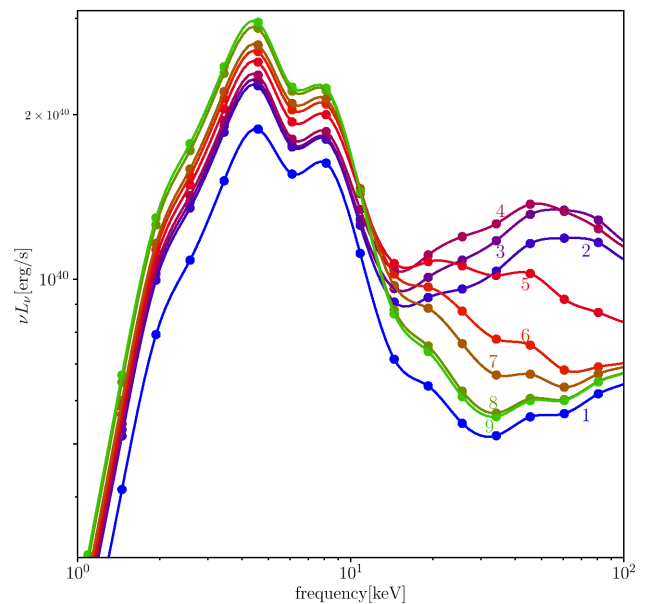

Fig. 6. Time evolution of the observed spectra in response to a flare that occurred at $t = t_0$ in the innermost zone viewed by a face-on observer (with $\theta_{\rm view} = 0°$). The color of the line changes from blue to red to green, as time goes on. The number near each line indicates the order of the time evolution: $t - t_0\,[M] = 50, 300, 350, 400, 450, 500, 550, 800$, and 1000 for the numbers 1 to 9, respectively. Note that the time of $1000\,M$ corresponds to ∼0.05 $(M/10\,M_\odot)$ s. (Color online)

the viewing angle; the smaller the view angle, the larger the variation amplitude. In the face-on case, the high-energy photon ($\gtrsim 20$ keV) counts begin to increase at $t = 1250\,M$ ($\sim t_0 + t_{\rm cross}$, between numbers 1 and 2 in figure 6), reach their maximum value at $t \sim 1400\,M$ (between numbers 4 and 5 in figure 6), and then decay to the steady-state values. The maximum amplitude of the variation is by a factor of ∼3 at a photon energy of ∼60 keV.

Why is the variability amplitude larger in hard X-rays to a face-on observer? This is because the hard X-ray emitting

region is much more compact than the soft X-ray emitting region (see figure 3), and because the hard X-rays can only reach nearly face-on observers and are blocked to observers at larger viewing angles (see the right panel of figure 2; see also figure 4).

Another noteworthy feature is the time delay in response among different energy bands: 60–100 keV photons rise more quickly than 15–30 keV photons, but the decay is similar among the different energy bins. This time delay between the arrival of harder and softer photons shown in figure 6 indicates that the hard photons generated in the funnel area close to the black hole are down-scattered at the funnel wall during the propagation to the outer boundary and thus their arrival is delayed. This mechanism is the same as that claimed by Kitaki et al. (2017). We may thus conclude that the spectral variability reflects the geometry of the hard X-ray emitting region.

We must admit, however, that it is practically impossible to detect such rapid hard X-ray variation with the existing or any planned X-ray satellites for the case with stellar-mass black holes. The timescale will be much longer, though, in cases with massive black holes: on the order of $\sim 400 M = 2 \times 10^4 (M/10^6 M_\odot)$ s. It might then be feasible to detect spectral variations with a future mission with good hard X-ray sensitivity. Application to massive black holes will be a future issue (see next section).

4 Discussion

In the present study we develop a new method for solving the Boltzmann radiation transport in the Schwarzschild space-time, incorporating the Compton scattering processes, and calculate the observed spectra of super-Eddington accretion flow and associated outflow. In this section we discuss the observational implications, compare with past simulation studies, and consider remaining future issues.

4.1 Observational implications: ULXs

The best objects we consider for the application of the present study are ultra-luminous X-ray sources (ULXs): compact, bright X-ray sources with luminosities comparable to or exceeding 10^{39} erg s^{-1} found in off-nuclear regions of nearby galaxies. There are several scenarios proposed to explain the nature of ULXs, but we favor the super-Eddington model (e.g., King et al. 2001; Watarai et al. 2001); that is, high luminosities of ULXs can be explained by super-Eddington accretion onto a stellar-mass black hole (with a mass of several tens of $M_\odot$ at most). One of the reasons for believing in the occurrence of super-Eddington accretion is the discovery of ULX pulsars, which

comprise magnetized neutron stars (although we do not consider ULX pulsars in this discussion). Another reason is that high-mass, binary companions are seemingly observed in some ULXs, and high mass-transfer rates via Roche-lobe overflow are expected there; see subsection 4.5 in the review by Kaaret, Feng, and Roberts (2017) and the references therein.

Rather unique ULX spectra, in comparison with the (sub-Eddington) Galactic X-ray binaries containing black holes, also support the super-Eddington model. There are several distinct spectral states known for the X-ray spectra of ULXs: the broadened disk (BD) state, hard UL state, soft UL state, the supersoft UL (SSUL) state, etc.; see, e.g., figure 2 of Kaaret, Feng, and Roberts (2017) for typical spectra. Interestingly, some of them (BD and hard UL states) show a rather broad spectral bump in the several to 10 keV range, which is consistent with the present study. To be more precise, hard UL spectra show rapid decay above several keV, whereas the typical X-ray spectrum extends over 10 keV and is very reminiscent of our calculated spectrum (see the right panel of figure 2). It is not clear yet why our model is consistent only with one particular state; this issue is left for future consideration. We just add that such a hard X-ray spectrum reflects very high temperature in the funnel region obtained by the GRRMHD simulation (see the discussion in the next subsection).

We should also mention that our spectra show rather weak soft X-ray emission compared with observations, especially below a few keV. This is because of the fluid model assumption (see subsection 2.1). The GRRMHD simulations started with an initial dense torus located at several to several tens of M, from which super-Eddington accretion flow is initiated; that is, a surrounding thin and cool disk (at $r >$ several tens of M), which should exist in real systems, is totally missing in the simulation so that the soft X-ray emission which would be produced in the thin and cool disk does not appear. This point needs to be improved in future studies (see also subsection 4.4).

4.2 Comparison with past simulation studies

We next discuss the connection with past simulation studies. The spectral study of super-Eddington accretors based on RHD simulation data was first performed by Kawashima et al. (2009, 2012), who calculated the observational X-ray spectra by using a Monte Carlo method and could reproduce the basic features of the observed X-ray spectra of ULXs, namely a spectral rollover around 5 keV and a hard power-law component extending up to 10 keV. They also pointed out the significance of bulk Comptonization and suggested that the face-on luminosities could exceed the luminosities of bright ULXs,

$L_x > 10^{40}\,\mathrm{erg\,s^{-1}}$. Such features are consistent with our results.

Kitaki et al. (2017) investigated the spectral properties of super-Eddington accretion flows with a Monte Carlo approach. Their results can explain the typical spectral features of ULXs, such as the hard excess above several keV. Although the accretion rate they adopted is near what we adopted, the spectral shapes are distinct between the two. Such differences arise because of the different fluid models. We find that the gas temperatures differ by a factor of two or more in the optically thick region near the black hole. Much larger differences are found in the funnel region; the temperature in their simulation is $\sim 10^8\,\mathrm{K}$ (see their figures 1 and 2), which is more than one order of magnitude lower than our fluid data, $\sim 10^9\,\mathrm{K}$, at most.

What causes such a difference? These major differences may arise from the inclusion/absence of GR effects and/or magnetic fields, since the data they use is based on 2D RHD simulation (which includes neither GR effects nor MHD processes). The GR effects provide deeper gravitational potential, which will give rise to a larger amount of energy released and thus result in higher gas temperatures. Magnetic fields can produce more energetic phenomena, such as magnetic reconnection, and may thus result in even higher gas temperatures. This is the main reason why the spectrum of our result is much harder than theirs. However, we should also point out that the observed spectral rollover around several keV is nicely reproduced by Kitaki et al. (2017), and thus supports relatively low ($\sim 10^8\,\mathrm{K}$) funnel temperatures.

Narayan, Saṃdowski, and Soria (2017) investigated the spectra of super-Eddington flows, incorporating both GR and magnetic field effects. Their spectrum from the model SANE (the green line in their figure 4) is also in good agreement with ULX BD-state spectra. Big differences from our results are that (i) they adopted a large outer boundary of the fluid data, i.e., $10^5\,M$, which is 400 times greater than ours, and that (ii) they approximately handled the Compton scattering by using the Kompaneets equation and isotropic scattering, while we handle it nearly perfectly by directly solving the Boltzmann equation except for the induced scattering. The difference in the outer boundary may affect the spectrum, as mentioned above (see also their figure 13), since the optical depth of the outflow can become more than our result and because the soft photons from the disk may increase.

The Kompaneets equation is derived under the assumption that the radiation field is isotropic and that the Fokker–Planck approximation would be a good approximation. In the funnel, the radiation field is highly anisotropic and the energy shift by the single scattering is very large, $\Delta\epsilon/\epsilon > 1$ (with ϵ being the photon energy). This fact should inevitably

affect the calculated spectra in the high-energy regime. They also showed a brightness map (see their figure 5), in which the funnel region is clearly seen when viewed from a low viewing angle. This feature is shared with our result.

It is notable that they estimated the gas temperature in a self-consistent fashion by considering the balance between radiation cooling and viscous heating, reporting that the observed spectra are significantly changed (see the red lines in their figure 4) by using the self-consistent temperature. In our method, the gas temperature is considered to be calculated in the GRRMHD simulation. For a more precise analysis of the spectra of ULXs, we should use the self-consistent temperature. This will be done in future work (see also subsection 4.4).

4.3 On the long-term spectral variability of ULXs

ULXs are known to exhibit rather complex X-ray spectral variations. A good example is displayed for the case with Ho IX X-1, see figure 3 of Vierdayanti, Mineshige, and Ueda (2010), where significant spectral variabilities were found on timescales of several to 100 d or even longer. Obviously, there is no one-to-one correspondence between the spectral shape and the X-ray luminosity. It seems that the broad soft X-ray component (in the range 0.5–5 keV) and the hard X-ray component (above 5 keV) vary independently. In some epochs the former totally dominates, with the latter being missing; in other epochs, the latter dominates with the former being weak. There also exists an epoch in which both components are bright. How can we understand this?

Since the timescale of the spectral variations of the sort we encounter here is much longer than the flaring timescale (see subsection 3.5), the variations cannot be of flare origin. We need to consider variations over a much wider spatial range. It is important to note in light of the present analysis that the soft, broad spectral component and the hard-band component have different origins: the latter originates from the funnel region, while the former from the disk and surrounding outflow. To understand the complex spectral variation of Ho IX X-1, we first need to require that it should be seen from nearly the face-on direction, since otherwise hard X-ray emission is difficult to observe. This agrees with the fact that its luminosity exceeds the Eddington luminosity, since mild beaming of radiation is one of the most prominent features of the super-Eddington flow. It then follows that the broad soft X-ray component and the hard X-ray component should change in a similar way, as long as the mass accretion rate ($\dot{M}$) is roughly constant in space. The existence of complex spectral variability thus means that

accretion should be time-dependent. If so, the expected variation timescale is the viscous timescale, namely

$$\tau_{\rm vis} \equiv \frac{1}{\alpha \Omega_{\rm K}} \left(\frac{R}{H}\right)^2 \simeq 10^{4.2}\,{\rm s} \left(\frac{\alpha}{0.1}\right)^{-1}$$
$$\times \left(\frac{M}{10\,M_\odot}\right) \left(\frac{R}{10^2\,R_{\rm S}}\right)^{3/2} \left(\frac{R/H}{10^2}\right)^2, \quad (7)$$

where the Keplerian angular frequency is $\Omega_{\rm K} \approx \sqrt{GM/R^3}$ and we estimated the aspect ratio of the standard-type disk at $R \sim 10^2 R_{\rm S}$ (with $R_{\rm S} = 2M$ being the Schwarzschild radius) to be

$$\frac{H}{R} \sim \frac{c_{\rm s}}{R\Omega_{\rm K}} \simeq 10^{-2} \left(\frac{T}{10^7\,{\rm K}}\right)^{1/2} \left(\frac{R}{10^2\,R_{\rm S}}\right)^{1/2} \quad (8)$$

(with $c_{\rm s}$ being the sound velocity) from the hydrostatic balance in the vertical direction (see sub-subsection 3.2.3 of Kato et al. 2008). We may thus conclude that $\dot{M}$ modulation over spatial ranges of several hundreds of $R_{\rm S}$ should be responsible for the observed spectral variabilities on timescales of several days or longer. Although we do not specify the origin of $\dot{M}$ variations here, this is a universal conclusion regardless of the cause of variability.

Here, we should again add a note of caution that a standard-type disk (which should be located around the initial torus) is not simulated in the present study. We thus perform a thought experiment here. Suppose that the mass injection rate suddenly increases at large radii, say at several hundreds of $R_{\rm S}$. Then, enhanced mass inflow is initiated there and propagates inward on the viscous timescale on the order of several days or even longer. Accordingly, the broad soft X-ray component first grows, as the $\dot{M}$ burst propagates inward, but the hard X-ray component does not respond immediately, since it is generated only in the funnel region. The hard X-ray component starts to rise only after the $\dot{M}$ burst reaches the innermost region, but in the meantime $\dot{M}$ in the outer parts may start to decay. Hence, there exists some time delay, comparable to the viscous timescale, between the rise of the soft X-ray component and that of the hard X-ray one. In this way, we can qualitatively understand the spectral behavior reported by Vierdayanti, Mineshige, and Ueda (2010), but more detailed, time-dependent study is left as a future issue.

4.4 Future prospects

We finally summarize some remaining issues and future work to inmprove the present code.

First, our code cannot currently calculate cases in which the central black hole is rotating. Since Kerr black holes seem to be more common than Schwarzschild black holes in the universe, we need to upgrade our code to solve radiative transfer around a spinning black hole. When the rotation of a black hole is prograde, the Blandford–Znajek mechanism will work to possibly produce an energetic jet. Narayan, Sądowski, and Soria (2017) reported the dependence of the spectra on the black hole spin; the spectrum will be notably harder when the black hole is rapidly spinning. This implies that the hardness ratio of the observed spectra may contain useful information regarding the black hole spin.

Second, induced scattering is not considered in our present code. Although this is a second-order (f^2) effect in Compton scattering, it may play an important role in the mildly optically thick region. In the effectively optically thick region (i.e., in the disk region), frequent absorption and re-emission take place, giving rise to blackbody radiation, and thus scatterings are not so important. In the effectively optically thin but Thomson thick region (i.e., near the funnel wall), in contrast the Compton scattering could be effective. Since the radiation field in the co-moving frame is highly collimated (i.e., more coherent in momentum space) in the funnel region, especially near the funnel wall, the induced scattering might not be negligible. Since the anisotropy of the radiation field is larger in the higher-energy band ($\gtrsim 10\,{\rm keV}$) in our calculation, the spectrum will be softer than the present result by the contribution of the induced scattering occurring near the funnel wall (with temperature $T \sim 10\,{\rm keV}$). Hence, we should more accurately calculate the Compton scattering in future work.

Third, Narayan, Sądowski, and Soria (2017) also reported the important fact that the emerged spectrum largely changes if we calculate the gas temperature self-consistently with radiation fields. The temperature at the innermost funnel region is much lower than that obtained by the GRRMHD simulation without such considerations, and thus the spectrum is softer. This ultimately requires the calculation of radiation field and fluid simultaneously.

Fourth, the initial torus should be placed at much larger radius so as to correctly calculate lower-energy spectra in particular. In our calculation, the disk is truncated at $r \sim 250\,M$ or less, whereas soft photons are expected to emerge from more distant regions (see figure 13 in Narayan et al. 2017). For this reason, a much larger calculation box size in the GRRMHD calculation is necessary. There is another reason why we should put an initial torus at as large a radius as possible. Kitaki et al. (2020) performed a long-term, large-box RHD simulation of a super-Eddingtion accretion flow and achieved a self-consistent (i.e., quasi-steady) steady accretion flow and outflow structure over a large spatial range at $r < 1200\,M$. They reported that the calculated outflow rate is much less, by one order of magnitude or even more, compared with the value obtained by
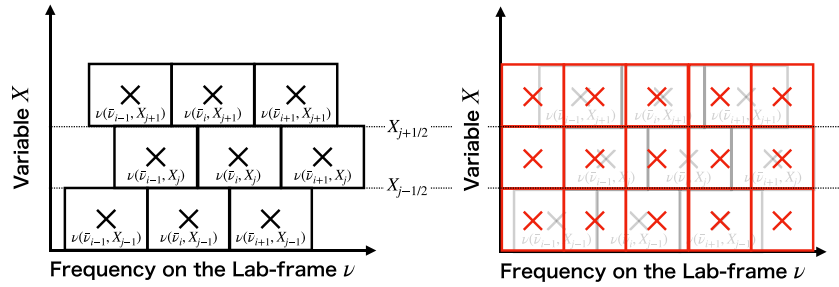
Fig. 7. Schematic diagrams showing the different 2D grid distributions, the frequency grid on the horizontal axis vs. that of some other quantity X on the vertical axis, in the co-moving regular grid (CRG; the black boxes in the left panel) and in the laboratory regular grid (LRG; the red boxes in the right panel). The grid distribution is regular in the LRG (right), but is not in the CRG (left). (Color online)

a previous study in which the quasi-steady state is achieved within a much smaller range (i.e., less than several tens of the Schwarzschild radius). Setting a much larger computation box is necessary to avoid artificial results.

Finally, it would be interesting to apply our methodology to investigate Fe Kα line diagnosis of the super-Eddington flow and moderately sub-Eddington accretion flow around massive black holes. Calculated line profile variations will be directly compared with future observations by the Athena satellite to explore the gas and radiation dynamics (and hopefully the space-time geometry as well) near the black hole (see, e.g., Dovciak et al. 2013). Incidentally, strong Fe line emission is not expected in the simulation data which we used in this study, since the disk surface is very hot, with temperatures exceeding $\sim 10^7$ K, so that metals including Fe will be fully ionized.

Acknowledgments

Appendix. Procedure for calculating numerical fluxes

In this appendix we explain some technical details of the conversion of the grid points between the laboratory frame and the fluid-rest frame.

Step 1

When calculating the numerical flux of the advection term, i.e., the left-hand side of equation (1), we should keep in mind that photon frequencies are calculated in the fluid-rest frame, while the frequency ν used in equation (1) is evaluated in the laboratory frame. The difficulty resides in the fact that the 2D distribution of the frequency grid and other grids of some quantity X (one of r, θ, φ, $\bar{\theta}$, or $\bar{\varphi}$) is not lattice shaped in the laboratory frame; see figure 7, and see also Nagakura, Sumiyoshi, and Yamada (2014). This is because the energy shift by the Doppler effect is a function of all the variables.

Suppose that we solve the numerical flux on the interface at $(j + 1/2)$ between the jth and the $(j + 1)$th cells of some variable X. The number of regular grids in the laboratory frame (LRG: laboratory regular grid) is set in such a way that each grid point should be in between the neighboring grid in meshes regular in the fluid-rest frame (CRG: co-moving regular grid). If the cell center ν_s in the LRG frame lies between the CRG cells of ν_i and ν_{i+1} (which we denote as $\bar{\nu}_i$ and $\bar{\nu}_{i+1}$ in the co-moving frame), the interpolated value, $f_{s,j}$ at ν_s, is calculated by

$$f_{s,j} = f_{i,j} + \frac{f_{i+1,j} - f_{i,j}}{\ln \nu_{i+1} - \ln \nu_i}(\ln \nu_s - \ln \nu_i). \tag{A1}$$

Step 2

After the interpolation, we calculate the advection terms of each differential X (other than the frequency differential) in the LRG by the second-order upwind method.

Step 3

The numerical fluxes we obtain in Step 2 are those in the LRG frame; however, we need to update the distribution function in the CRG frame. Therefore, we should interpolate again now from the LRG frame to the CRG frame. Since the interface of an LRG cell (denoted as s) lies between the ith and $(i + 1)$th CRG cells, the numerical flux in the X-direction in the sth cell in the LRG, $F_{s,\mathrm{LRG}}^{j+1/2}$, should be split into these two CRG cells. Here, we define the CRG

numerical fluxes in the cell surface $(j + 1/2)$, $(j - 1/2)$ of the jth cell of a variable X, $F_{i,\mathrm{CRG}}^{j+}$, as

$$
F_{i,\mathrm{CRG}}^{j+} = \sum_{s \in \Lambda_i^j} \frac{\ln \min(\nu_{s+1/2}, \nu_{i+1/2}^j) - \ln \max(\nu_{s-1/2}, \nu_{i-1/2}^j)}{\ln \nu_{i+1/2}^j - \ln \nu_{i-1/2}^j}
$$
$$
\times F_{s,\mathrm{LRG}}^{j+1/2}, \tag{A2}
$$

$$
F_{i,\mathrm{CRG}}^{j-} = \sum_{s \in \Lambda_i^j} \frac{\ln \min(\nu_{s+1/2}, \nu_{i+1/2}^j) - \ln \max(\nu_{s-1/2}, \nu_{i-1/2}^j)}{\ln \nu_{i+1/2}^j - \ln \nu_{i-1/2}^j}
$$
$$
\times F_{s,\mathrm{LRG}}^{j-1/2}, \tag{A3}
$$

$$
\Lambda_i^j = [s | (\nu_{i-1/2}^j, \nu_{i+1/2}^j) \cap (\nu_{s-1/2}, \nu_{s+1/2}) \neq \varnothing], \tag{A4}
$$

where the quantity ν_i^j is the frequency in the laboratory frame of the ith cell of the frequency (which is defined in the comoving frame) and the jth cell of the variable X. It is notable that the numerical fluxes $F_{i,\mathrm{CRG}}^{j+}$ and $F_{i,\mathrm{CRG}}^{(j+1)-}$ are the flux at the interface at $(j + 1/2)$ but are not always the same, since the numerical fluxes also depend on physical quantities in the $(i + 1, j)$, $(i - 1, j)$, etc. cells because of the Doppler (frequency) shift.

Step 4

After calculating the numerical flux in the CRG, we update the primitive value f (distribution function) following the equation

$$
f_{i,j}(t + \Delta t) = f_{i,j}(t) - \frac{\Delta t}{\Delta x_j}(F_{i,\mathrm{CRG}}^{j+} - F_{i,\mathrm{CRG}}^{j-}). \tag{A5}
$$

Note that the grid-based Boltzmann solver inevitably suffers from incorrectness for the dynamic diffusion problem. Suppose the interacting fluid has velocity v and a reasonably large optical depth τ. In this case, the radiation moves with the same velocity as the fluid and diffuses by an amount determined by the optical depth. This is the dynamic diffusion problem. In the case of the grid-based Boltzmann solver, the limitation of resolution for the direction and the time make it difficult to solve the diffusion–advection problem correctly. To avoid this issue, we adopt a method analogous to that described by equation (34) in Ohsuga and Takahashi (2016), where the numerical flux is made by a combination of numerical flux from the Boltzmann equation and that from the assumption that the radiation moves with the fluid.

References

Dolence, J. C., Gammie, C. F., Mościbrodzka, M., & Leung, P. K. 2009, ApJS, 184, 387

Done, C., Gierliński, M., & Kubota, A. 2007, A&A Rev., 15, 1

Dovciak, M., et al. 2013, arXiv:1306.2331

Falanga, M., Belloni, T., Casella, P., Gilfanov, M., Jonker, P., & King, A. eds. 2015, The Physics of Accretion onto Black Holes (New York: Springer)

Galeev, A. A., Rosner, R., & Vaiana, G. S. 1979, ApJ, 229, 318

Haardt, F., & Maraschi, L. 1991, ApJ, 380, L51

Kaaret, P., Feng, H., & Roberts, T. P. 2017, ARA&A, 55, 303

Kato, S., Fukue, J., & Mineshige, S. 2008, Black-Hole Accretion Disks: Towards a New Paradigm (Kyoto: Kyoto University Press)

Kawashima, T., Ohsuga, K., Mineshige, S., Heinzeller, D., Takabe, H., & Matsumoto, R. 2009, PASJ, 61, 769

Kawashima, T., Ohsuga, K., Mineshige, S., Yoshida, T., Heinzeller, D., & Matsumoto, R. 2012, ApJ, 752, 18

Kinch, B. E., Schnittman, J. D., Kallman, T. R., & Krolik, J. H. 2016, ApJ, 826, 52

King, A. R., Davies, M. B., Ward, M. J., Fabbiano, G., & Elvis, M. 2001, ApJ, 552, L109

Kitaki, T., Mineshige, S., Ohsuga, K., & Kawashima, T. 2017, PASJ, 69, 92

Kitaki, T., Mineshige, S., Ohsuga, K., & Kawashima, T. 2021, PASJ, 73, 450

Liang, E. P., & Nolan, P. L. 1984, Space Sci. Rev., 38, 353

Martocchia, A., & Matt, G. 1996, MNRAS, 282, L53

Miniutti, G., & Fabian, A. C. 2004, MNRAS, 349, 1435

Mościbrodzka, M., Falcke, H., Shiokawa, H., & Gammie, C. F. 2014, A&A, 570, A7

Nagakura, H., Sumiyoshi, K., & Yamada, S. 2014, ApJS, 214, 16

Narayan, R., Sądowski, A., & Soria, R. 2017, MNRAS, 469, 2997

Oda, M., Gorenstein, P., Gursky, H., Kellogg, E., Schreier, E., Tananbaum, H., & Giacconi, R. 1971, ApJ, 166, L1

Ohsuga, K., & Takahashi, H. R. 2016, ApJ, 818, 162

Pozdnyakov, L. A., Sobol, I. M., & Syunyaev, R. A. 1977, Soviet Ast., 21, 708

Ryan, B. R., & Dolence, J. C. 2020, ApJ, 891, 118

Rybicki, G. B., & Lightman, A. P. 1979, Radiative Processes in Astrophysics (Chichester: Wiley)

Shibata, M., Nagakura, H., Sekiguchi, Y., & Yamada, S. 2014, Phys. Rev. D, 89, 084073

Sumiyoshi, K., & Yamada, S. 2012, ApJS, 199, 17

Takahashi, H. R., Mineshige, S., & Ohsuga, K. 2018, ApJ, 853, 45

Takahashi, R., & Umemura, M. 2017, MNRAS, 464, 4567

Vierdayanti, K., Mineshige, S., & Ueda, Y. 2010, PASJ, 62, 239

Watarai, K., Mizuno, T., & Mineshige, S. 2001, ApJ, 549, L77